

Dynamic multi-axial behavior of shape memory alloy nanowires with coupled thermo-mechanical phase-field models

R. P. Dhote · R. N. V. Melnik · J. Zu

Received: 13 July 2013 / Accepted: 22 March 2014 / Published online: 18 April 2014
© The Author(s) 2014

Abstract The objective of this paper is to provide new insight into the dynamic thermo-mechanical properties of shape memory alloy (SMA) nanowires subjected to multi-axial loadings. The phase-field model with Ginzburg–Landau energy, having appropriate strain based order parameter and strain gradient energy contributions, is used to study the martensitic transformations in the representative 2D square-to-rectangular phase transformations for FePd SMA nanowires. The microstructure and mechanical behavior of martensitic transformations in SMA nanostructures have been studied extensively in the literature for uniaxial loading, usually under isothermal assumptions. The developed model describes the martensitic transformations in SMAs based on the equations for momentum and energy with bi-directional coupling via strain, strain rate and temperature. These governing equations of the thermo-mechanical model are numerically solved simultaneously for different

external loadings starting with the evolved twinned and austenitic phases. We observed a strong influence of multi-axial loading on dynamic thermo-mechanical properties of SMA nanowires. Notably, the multi-axial loadings are quite distinct as compared to the uniaxial loading case, and the particular axial stress level is reached at a lower strain. The SMA behaviors predicted by the model are in qualitative agreements with experimental and numerical results published in the literature. The new results reported here on the nanowire response to multi-axial loadings provide new physical insight into underlying phenomena and are important, for example, in developing better SMA-based MEMS and NEMS devices

Keywords Shape memory alloy · Thermo-mechanical coupling · Multi-axial loading · Phase-field model · Nanowire

R. P. Dhote (✉) · J. Zu
Mechanical and Industrial Engineering, University of
Toronto, 5 King's College Road, Toronto, ON M5S-3G8,
Canada
e-mail: rakesh.dhote@mail.utoronto.ca

R. P. Dhote · R. N. V. Melnik
M2NeT Laboratory, Wilfrid Laurier University, 75
University Avenue, Waterloo, ON N2L-3C5, Canada

R. N. V. Melnik
Universidad Carlos III de Madrid, Avenida de la
Universidad 30, E28911 Leganes, Spain

1 Introduction

The unique shape recovering characteristics, high energy density, and high actuation strain of shape memory alloys (SMAs) make them ideal candidates for use in macro-, micro-, and nano- scale actuators, sensors and transducers [1–6]. The shape recovering characteristics give rise to the complex nonlinear mechanical behavior of these materials. The complexity arises because of the coupling between thermal

and mechanical (or structural) physics, and due to martensitic transformations (MTs)

SMA have been extensively studied (see e.g., [7–11]) and used in commercial applications [10, 12–16]. Most of the applications to date are designed to exploit the uniaxial properties of SMA wires, and there is a vast literature on experimental data of ubiquitous uniaxial tensile tests. However, in many of the applications in fields such as bioengineering and nanotechnology, SMA specimens are often subjected to multi-axial loadings [14, 17–19]. For such advanced applications, further knowledge of multi-axial properties of SMAs is required, yet very few experimental data on multi-axial response of SMA specimens are available in the literature [20–26]. Tokuda et al. [20] and Sittner et al. [21] conducted combined tension-torsion experiments on thin wall Cu-based polycrystalline SMA specimens and reported a coupling between tension and torsion during forward and reverse transformations that can be used to control the axial strain via torque and vice versa. The variation in mechanical properties subjected to multi-axial loadings has been experimentally confirmed by Lim and McDowell [22], and Bouvet et al. [23]. McNaney et al. [24] investigated variations in mechanical responses during biaxial tension-torsion experiments on NiTi thin wall tubes subjected to various loading and unloading paths under isothermal conditions. Recently, Lavernhe-Taillard et al. [25] and Grabe and Bruhns [26] conducted several multi-axial tension-torsion experiments on thin wall NiTi tubes which showed significant differences in mechanical behavior of SMAs. The above studies suggested that the variation in mechanical response stems from the nucleation of energetically favorable martensitic variants to applied loadings. However, most of the above studies focused on experimental stress–strain curves with little focus on underlying MTs.

The controlled experiments in SMAs are complex because of required simultaneous control of stress and deformation in time and space. In addition, the multi-axial experimental setups are expensive and time consuming. Hence, models have been developed to predict the properties of SMA structures for design and optimization. Several modeling approaches have been developed to predict the SMA properties. The majority of the models in the literature focused on uniaxial tensile test data. Extensive reviews of such models for SMAs have been discussed in [8–10, 27–29]. With the

need of predicting multi-axial properties of SMAs for advanced technological applications, there has been an increasing focus on the development of multi-axial models [30–35]. Tokuda et al. [30] proposed a two dimensional micromechanical model based on crystal plasticity and the deformation gradient to describe thermo-mechanical behavior in polycrystalline Cu-based SMAs subjected to multi-axial loadings. Bouvet et al. [31] presented a phenomenological model taking into account tension-compression asymmetry for predicting pseudoelastic behavior of SMAs under multi-axial loadings using two phase transformations surfaces. Thiebaud et al. [32] used a phenomenological model developed by Raniecki et al. [36] to simulate internal loops in order to characterize the stiffness and the damping effect by an equivalent complex Youngs modulus approach under static strain offsets. A rate-independent crystal mechanics based model developed by Pan et al. [33] is used to quantitatively predict the experimental response of the NiTi rod under tension-torsion loading conditions. Arghavani et al. [34] presented a phenomenological model, based on the framework of irreversible thermodynamics, that uses stress-induced martensite as scalar internal variable and the preferred direction of the variants as independent tensorial internal variable to predict the experimentally observed SMA behavior subjected to multi-axial loadings. Recently, Saleeb et al. [35] proposed a fully general three dimensional SMA model, based on partitioning of the stored and dissipated mechanical energies by utilizing the notion of multiplicity of inelastic mechanisms, to capture numerous uniaxial and multi-axial experimental responses of SMA material. All the above studies indicate the importance of multi-axial loadings on the SMA properties.

We are interested here specifically in the phase-field (PF) models that have emerged as a powerful computational approach for modeling microstructures and mechanical properties of solid-to-solid phase transformations in SMAs [37–47]. This approach provides a unified framework that allows to describe stress and temperature induced phase transformations, including their dynamics in the variational setting. The PF models have been used to study microstructure and mechanical properties of meso- and nano-scale SMA specimens. Bouville and Ahluwalia [45] used the PF model with the Ginzburg–Landau free energy to study the microstructure in constrained nanostructures and mechanical properties of infinite length nanowires

subjected to axial loading. They observed size dependent properties and size effects in nanostructures. Ahluwalia et al. [43] carried out the three dimensional simulations to study the axial properties of nanosize samples with periodic boundary conditions for the cubic-to-tetragonal phase transformations in the FePd crystals. They investigated changes in the stress–strain behavior as a function of strain rate. Idesman et al. [48] studied the evolution of microstructures in periodic nanosized three dimensional NiAl samples using the advanced potential developed by Levitas and Preston [42]. Although SMAs possess strong temperature dependent properties [10], most of the above studies were carried out under the assumption of isothermal conditions. In the series of papers by Melnik and coworkers [38, 39, 49–53] a coupled thermo-mechanical PF models have been used to study the dynamics of SMAs based on the Ginzburg–Landau free energy. Nevertheless, most of the studies focused on the mechanical behavior of SMA structures under uniaxial loadings only. However, as mentioned above, important applications exist where the SMA structure may induce multi-axial loading during interactions with its environment.

In this paper, the objective is to study the properties of finite length nanowires with a fully coupled nonlinear thermo-mechanical formulation under multi-axial loadings. We use the mesoscale PF model developed in our earlier work [54, 55] to study the SMA dynamics based on the Ginzburg–Landau free energy of 2D square-to-rectangular phase transformations. The details of size dependent properties and size effects in SMA nanostructures using the developed coupled thermo-mechanical model have been discussed in Dhote et al. [53]. In Dhote et al. [56], we performed the first fully coupled thermo-mechanical multi-axial loadings experiments on finite length SMA nanowires using the PF model in the dynamic setting and presented preliminary studies on the behavior of SMA nanowire initially in twinned microstructure. Here, we carry out a detailed study and conduct series of complex multi-axial numerical experiments to understand the microstructure evolution and its impact on stress–strain properties of SMA nanowires initially in twinned and austenite phases.

The rest of the paper is organized as follows. In Sect. 2, we present a general mathematical framework for modeling the SMA dynamics for 2D square-to-rectangular phase transformations. We conduct a

series of numerical experiments with different multi-axial loading conditions on SMA nanowires. In Sect. 3, we investigate the effect of microstructure on the thermo-mechanical behavior of SMAs upon multi-axial loadings. Finally, Sect. 4 summarizes the results and discusses the scope for future work.

2 SMA dynamics

The mathematical model to study the SMA dynamics is based on a mesoscale model analyzed in detail numerically in our earlier works [53, 55]. In this work, our focus is on the thermo-mechanical behavior of FePd nanowires subjected to multi-axial loadings based on microstructure evolution. The FePd material has a high temperature, high-symmetry face centered cubic (FCC) austenite phase, as well as low temperature, low-symmetry face-centered tetragonal (FCT) martensitic phases (with tetragonal crystal aligned with elongated side along three rectilinear directions). The material exhibits cubic-to-tetragonal martensitic phase transformations under thermal and mechanical loadings. The martensitic phase transformation is a highly nonlinear phenomenon. In addition, the coupled thermo-mechanical model and three dimensional simulations make computations challenging [39, 50].

To make the computation tractable, we study the MTs using the simplified 2D square-to-rectangular representative phase transformations under the assumption that the deformation in the out-of-plane direction is constant. The effect of the third direction deformation on microstructure evolution has been reported elsewhere with the 3D dynamic thermo-mechanical phase-field models [57, 58]. However, here we focus on the 2D square-to-rectangular phase transformations in SMAs, where the square represents the austenite phase A and the rectangles represent the martensitic variants M⁺ and M[−] (with rectangle length aligned along two perpendicular axes). As the austenite and martensite variants have different energies and prevail at different temperatures, the phase transformations in SMA can be modeled by using the Ginzburg–Landau free energy [52, 54].

As per Falk [59], strains in the domain can be used to describe different phases in the domain. The strain components which directly contribute to PT are called order-parameters (ops), and the others are called non-OPs (nop). For square-to-rectangular PT, the

deviatoric strain e_2 serves as an OP. The free energy \mathcal{F} of PT is described as

$$\mathcal{F} = \mathcal{F}_{\text{op}} + \mathcal{F}_{\text{nop}} + \mathcal{F}_{\text{gradient}}, \tag{1}$$

where \mathcal{F}_{op} is the energy part due to the OPs, which contributes to MT as per the Landau–Devonshire theory, \mathcal{F}_{nop} is the energy part due to non-OPs, which contributes to the bulk and shear energy, and $\mathcal{F}_{\text{gradient}}$ is the energy part which contributes to the energy cost required to maintain different domain phases in a domain and interface formed between physical boundaries and domain. The gradient energy term (or the Ginzburg energy) maintains a non-zero width in austenite-martensite and martensite–martensite interfaces, and prevents the system from creating an infinite number of interfaces (e.g. [60]). The gradient term introduces a nano length scale width of a domain wall in the model ([41, 43] and references within). As a result, the Landau–Ginzburg theory has been applied to nanoferroelastic and nanoferroelectric systems to study the dynamic behavior of nanostructures [45, 61].

The free energy components in (1) for 2D square-to-rectangular PTs are defined as

$$\begin{aligned} \mathcal{F}_{\text{op}} &= \frac{a_2}{2} \left(\frac{\theta - \theta_m}{\theta_m} \right) e_2^2 - \frac{a_4}{4} e_2^4 + \frac{a_6}{6} e_2^6, \\ \mathcal{F}_{\text{nop}} &= \frac{a_1}{2} e_1^2 + \frac{a_3}{2} e_3^2, \\ \mathcal{F}_{\text{gradient}} &= \frac{k_g}{2} \left[\left(\frac{\partial e_2}{\partial x_1} \right)^2 + \left(\frac{\partial e_2}{\partial x_2} \right)^2 \right], \end{aligned} \tag{2}$$

where e_1, e_2 and e_3 are the hydrostatic, deviatoric and shear strain respectively defined as $e_1 = (\epsilon_{xx} + \epsilon_{yy})/\sqrt{2}$, $e_2 = (\epsilon_{xx} - \epsilon_{yy})/\sqrt{2}$, $e_3 = (\epsilon_{xy} + \epsilon_{yx})/2$, with $\epsilon_{ij} = [(\partial u_i/\partial x_j) + (\partial u_j/\partial x_i)]/2$ being the Cauchy–Lagrange infinitesimal strain tensor; $u_i, i = 1, 2$ are displacements along x_1 and x_2 directions, respectively (refer to Fig. 2), θ is the material temperature, θ_m is the austenite-martensite phase transformation temperature, a_i are the material constants, and k_g is the Ginzburg coefficient. As the maximum strain induced in the domain is $\leq 3\%$ (refer to Table 1), a geometric linear kinematic (infinitesimal) relationship is a simple and convenient assumption. The influence of large strain (geometric non-linear) definition (large strain and material rotation) in the model and its effect on the phase transformations, due to finite rotation, have been highlighted by Clayton and Knap [62], Hildebrand and Miehe [63], Levin et al. [64] and in references [65, 66].

Table 1 Numerical experiments—multi-axial loading patterns

Set no.	Expt. no.	Axial			Bending		
		χ_a (%)	t_{sa} (ns)	t_{la} (ns)	χ_b (%)	t_{sb} (ns)	t_{lb} (ns)
I	1	3	0	1	0	0	0
	2	0	0	0	3	0	1
	3	3	0	1	3	0	1
II	4	3	0	1	3	1/8	1/6
	5	3	0	1	3	1/5	1/4
	6	3	0	1	3/2	1/5	1/4

As discussed above, the deviatoric strain e_2 is selected as the order parameter to distinguish different phases in a domain. The austenite phase exists when strains in both directions are equal i.e. $e_2 = 0$ ($\partial u_1/\partial x_1 = \partial u_2/\partial x_2$). The martensite variants M+ exist when the strain in x_1 direction is greater than strain in x_2 direction i.e. $e_2 > 0$ ($\partial u_1/\partial x_1 > \partial u_2/\partial x_2$), and the martensite variant M– exist when the strain in x_2 direction is greater than strain in x_1 direction i.e. $e_2 < 0$ ($\partial u_1/\partial x_1 < \partial u_2/\partial x_2$). With the free energy given by (1), the SMA behavior is captured by the mathematical model that couples the structural and thermal fields using the conservation equations of mass, momentum, and energy in the way described previously in Melnik et al. [49].

The governing equations of SMA dynamics are obtained by minimizing the total energy in a domain. The kinetic energy \mathcal{K} , and the dissipation functional \mathcal{R} are given by

$$\mathcal{K}(t) = \frac{\rho}{2} v_i^2, \quad \text{and} \quad \mathcal{R}(u_i, t) = \frac{\eta}{2} \dot{u}_{i,j}^2, \tag{3}$$

where ρ is the mass density, η is the dissipation coefficient, $v_i (= \dot{u}_i)$ is the velocity in the i th direction, and $\dot{u}_{i,j}$ refers to the differentiation of velocity u_i in j direction, with $i, j = 1, 2$ respectively.

The Lagrangian \mathcal{L} and the Hamiltonian \mathcal{H} of the system are defined as

$$\mathcal{L} = \mathcal{K}(t) - \mathcal{F} - \mathcal{R}(u_i, t), \tag{4}$$

$$\mathcal{H} = \int_0^t \int_{\Omega} (\mathcal{L} - f_i u_i) d\Omega dt, \tag{5}$$

where f_i are the mechanical loadings in the i th direction, Ω is the SMA domain, and $[0, t]$ is the time span.

Using the Hamiltonian principle, the structural (or mechanical) dynamics equations are obtained as

$$\rho \frac{\partial^2 u_i}{\partial t^2} = \sum \frac{\partial \sigma_{ij}}{\partial x_j} + \sigma_{g_i} + \eta \nabla^2 v_i + f_i, \tag{6}$$

where $\sigma_{ij} = \partial/\partial \epsilon_{ij}(\mathcal{F}_{op} + \mathcal{F}_{nop})$, and $\sigma_{g_i} = \partial/\partial \epsilon_{ij}(\mathcal{F}_g)$ [53]. On simplification, we obtain the stress tensor components as

$$\sigma_{11} = \frac{1}{\sqrt{2}} \left[a_1 e_1 + a_2 \left(\frac{\theta - \theta_m}{\theta_m} \right) e_2 - a_4 e_2^3 + a_6 e_2^5 \right], \tag{7}$$

$$\sigma_{12} = \frac{1}{2} a_3 e_3, \tag{8}$$

$$\sigma_{21} = \sigma_{12}, \tag{9}$$

$$\sigma_{22} = \frac{1}{\sqrt{2}} \left[a_1 e_1 - a_2 \left(\frac{\theta - \theta_m}{\theta_m} \right) e_2 + a_4 e_2^3 - a_6 e_2^5 \right], \tag{10}$$

and the σ_{g_i} components are

$$\sigma_{g_1} = k_g \left[-\frac{\partial^4 u_1}{\partial x_1^4} - \frac{\partial^4 u_1}{\partial x_1^2 \partial x_2^2} + \frac{\partial^4 u_2}{\partial x_1^3 \partial x_2} + \frac{\partial^4 u_2}{\partial x_1 \partial x_2^3} \right], \tag{11}$$

$$\sigma_{g_2} = k_g \left[\frac{\partial^4 u_1}{\partial x_1^3 \partial x_2} + \frac{\partial^4 u_1}{\partial x_1 \partial x_2^3} - \frac{\partial^4 u_2}{\partial x_1^2 \partial x_2^2} - \frac{\partial^4 u_2}{\partial x_2^4} \right]. \tag{12}$$

Equations (7–10) define the material behavior in square-to-rectangular PTs. The fourth order terms in (11–12) are the extra stress terms which correspond to the strain gradient terms in the free energy \mathcal{F} , and represent the domain walls between different phases of the martensites.

The governing equation of the thermal field is obtained by the conservation laws of internal energy [49] as

$$\rho \frac{\partial e}{\partial t} - \sigma^T : \nabla v + \nabla \cdot q = g, \tag{13}$$

where $q = -\kappa \nabla \theta$ is the Fourier heat flux vector (as mentioned in Melnik et al. [39], the hyperbolic Cattaneo-Vernotte law may be more appropriate in some cases), κ is the heat conductance coefficient of the material, and g is the thermal loading. The internal energy is connected with the potential energy constructed above via the Helmholtz free energy Ψ as

$$e = \Psi(\theta, \epsilon) - \theta \frac{\partial \Psi(\theta, \epsilon)}{\partial \theta}, \tag{14}$$

$$\Psi(\theta, \epsilon) = \mathcal{F} - C_v \theta \ln \theta,$$

where C_v is the specific heat of a material.

On substituting (14) in the (13), the governing equation of the thermal field in two dimensions can be given as

$$\rho C_v \frac{\partial \theta}{\partial t} = \kappa \left(\frac{\partial^2 \theta}{\partial x^2} + \frac{\partial^2 \theta}{\partial y^2} \right) + a_2 \frac{\theta}{\theta_m} e_2 \frac{\partial e_2}{\partial t} + g. \tag{15}$$

The second term on the right hand side of (15) is a non-linear term, which couples temperature, deformation gradient (strain), and rate of deformation gradient (strain rate). Hence the overall system of (6) and (15) describes the non-linear thermo-mechanical coupled behavior of SMAs via θ, e_2 , and \dot{e}_2 .

In Dhote et al. [53], we used (6) and (15) to study the behavior of SMA nanostructures of different sizes. We also captured the martensitic transformation suppression phenomenon and size dependent properties observed experimentally and numerically (see e.g., [45, 67]) by using the developed thermo-mechanical model. We also conducted the uniaxial loadings on the nanowire under the assumption of isothermal conditions. The results were in qualitative agreement with the results obtained from uncoupled models (e.g. [45]). We also obtained qualitative agreement in temperature evolution during dynamic loading and unloading of the SMA specimen with the experimental work conducted by Gadaj et al. [68] and Pieczyska et al. [69, 70] using the developed thermo-mechanical model. In Dhote et al. [56], we carried out the preliminary studies of nanowire behavior subjected to multi-axial loadings with nanowire initially in twinned martensitic phase. We extend the study here with additional complex multi-axial loading experiments starting with nanowire initially in twinned phase and a new set of simulations starting with nanowire in austenite phase. In the remainder of this paper, we focus on the results of numerical simulations of SMA nanowires subjected to multi-axial loadings. Before we proceed, we remark that currently our model does not account explicitly for surface effects [71], however the developed framework can be easily extended to incorporate them.

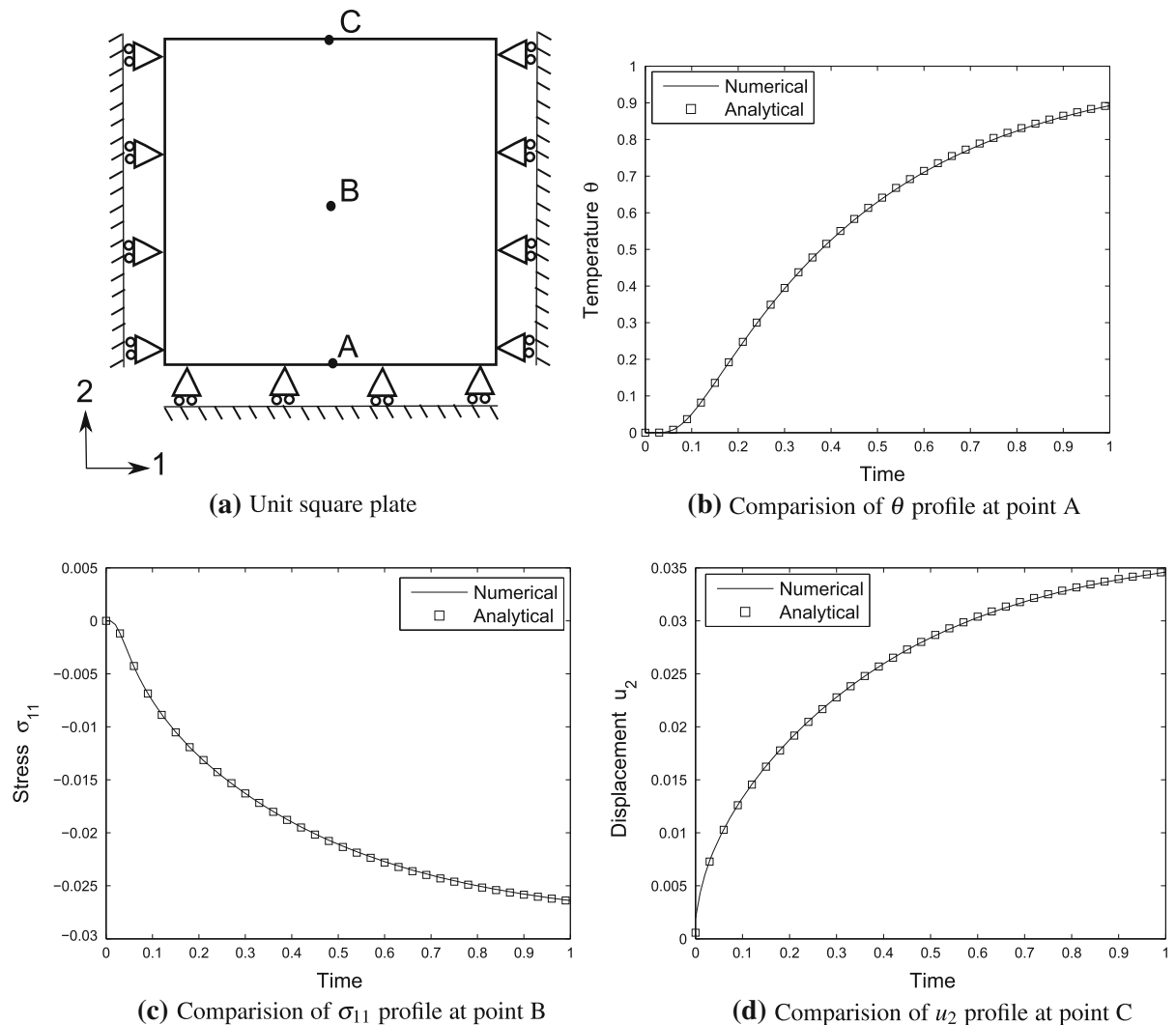


Fig. 1 Comparison of dimensionless numerical and analytical results [73] for a test problem on a unit square plate

3 Numerical simulations

The Eqs. (6) and (15) are rescaled in the spatio-temporal domain for numerical convenience and solved numerically using the finite element method. We have implemented the equations in the Comsol Multi-physics software [72] by first splitting the fourth order differential terms into two second order differential terms. As the experimental studies of dynamic multi-axial behaviors in SMA nanowires are not available in the literature, we validate the model at different stages as described in the following sections. We first verify the developed model and its numerical

implementation using a test problem [73]. A unit square plate insulated and constrained in the normal directions on the three edges, and subjected to sudden unit heating on the fourth edge as schematically depicted in Fig. 1a. We reduce the system of (6) and (15) to the homogeneous thermo-elastic equations [74] under the following assumptions:

- the unit square plate is in plane strain condition,
- the higher power strain terms a_4 and a_6 , accounting for the phase transformations, are neglected,
- the phase transformation is homogeneous i.e. the Ginzburg term k_g is neglected, and

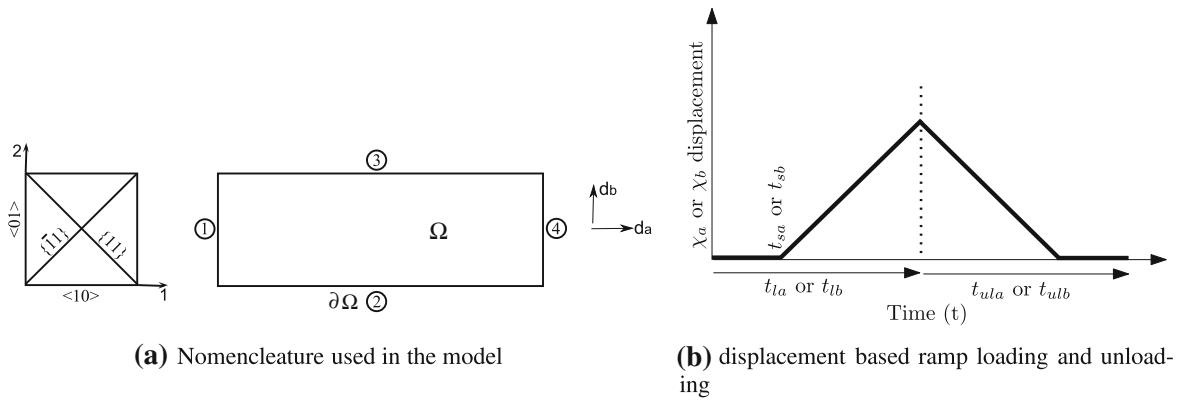


Fig. 2 Schematic indicating **a** direction, plane, and boundary ($\partial\Omega$) nomenclature in the nanowire domain (Ω) and loadings during multi-axial loadings [56], and **b** displacement based ramp loading and unloading

- the second term on the right hand side of (15) is neglected.

The resulting equations are solved numerically, as mentioned above, and the dimensionless results are compared with the analytical solutions in Park and Banerjee [73]. The dimensionless temperature θ , stress σ_{11} , and displacement u_2 profiles at the points A, B, and C, respectively in Fig. 1 are in agreement with the analytical homogeneous solutions of thermo-elasticity. We also solved the non-homogeneous system of equations with dynamic thermo-mechanical coupling. The results are in qualitative agreement with experimental and numerical results as described in detail in the subsequent sections.

Next, we perform the numerical experiments on rectangular domain (Ω) nanowires of dimension 1000×200 nm with sides parallel to $\langle 10 \rangle$ and $\langle 01 \rangle$ directions defined with reference to the austenite phase as shown in Fig. 2a. The FePd material parameters used for the simulations are (see e.g., [45]):

$$a_1 = 140 \text{ GPa}, a_3 = 280 \text{ GPa}, a_2 = 212 \text{ GPa}, a_4 = 17 \times 10^3 \text{ GPa}, a_6 = 30 \times 10^6 \text{ GPa}, \theta_m = 265 \text{ K}, \eta = 0.025 \text{ Nsm}^{-2}, k_g = 3.5 \times 10^{-8} \text{ N}, C_v = 350 \text{ Jkg}^{-1} \text{ K}^{-1}, \text{ and } \kappa = 78 \text{ Wm}^{-1} \text{ K}^{-1}.$$

3.1 Microstructure evolution

The series of numerical simulations have been conducted to study the response of the nanowire to multi-axial loadings. The nanowires are subjected to different temperatures θ_{init} for sufficiently long time to evolve into the twinned [56] and austenite phases. The strategy adopted here is to first evolve the

microstructure in the domain and then use the evolved microstructure as an initial condition in the multi-axial loading simulations.

The boundary and initial conditions used during microstructure evolutions are

$$u_i|_{(\partial\Omega,t)} = 0, \quad \nabla u_i \cdot \mathbf{n}|_{(\partial\Omega,t)} = 0, \quad \nabla \theta \cdot \mathbf{n}|_{(\partial\Omega,t)} = 0, \\ \theta|_{(\Omega,t=0)} = \theta_{init} \mathbf{K}, \quad u_i|_{(\Omega,t=0)} = \text{white noise}, \quad (16)$$

where \mathbf{n} is the normal vector to the boundary. During microstructure evolution, the mechanical boundary conditions are set to $\mathbf{u} = \mathbf{0}$ on all the boundaries. All the simulations in the paper have been conducted under the assumption of adiabatic temperature conditions on all the boundaries. The simulations have been performed on the finite domain size with constrained or stress-free boundary conditions. The nanowire is set to the initial temperature $\theta_{init} = 250\text{K}$, and 270 K to evolve into the twinned, and austenite phases respectively.

The microstructures are allowed to evolve till it gets stabilized over a long simulation time. The evolved microstructures is shown in Fig. 3. The red and blue colors represent the M+ and M− martensitic variants and the green color represents the A phase. Figure 3a shows the evolved twinned martensite phase, and Fig. 3b shows the evolved austenite phase. The evolved microstructure in twinned martensite is self-accommodated and forms domain walls oriented in $\{11\}$ or $\{\bar{1}\bar{1}\}$ planes to minimize the energy [75–77]. During the microstructure evolution, the temperature increase is observed due to the insulated boundary conditions and thermo-mechanical coupling between temperature θ , strain e_2 , and strain rate \dot{e}_2 .

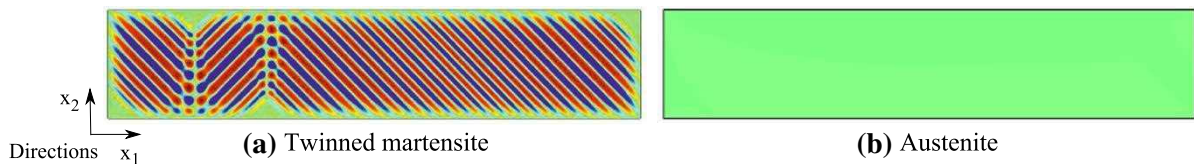


Fig. 3 (Color online) Evolution of **a** twinned [56], and **b** austenite microstructure in the nanowire (*red and blue* indicates martensite variants and *green* indicates austenite)

3.2 Multi-axial loading

We now perform the multi-axial loading simulations on the evolved microstructure from the previous subsection. We consider the evolved microstructure as an initial condition to the loading experiments. In order to investigate the response of the nanowire to different loading patterns, we carried out a series of numerical experiments as described in Table 1. The simple experiments with axial (experiment 1) and bending (experiment 2) loads have been first conducted and the response of nanowire has been compared with multi-axial loadings (experiment 3, i.e. axial and bending loads applied simultaneously). Next, different patterns of multi-axial loadings have been applied to study the nanowire response to complex loadings. The initial and boundary conditions for all the simulations are:

$$u_i|_{(\partial\Omega=1,t)} = 0, \quad \nabla u_i \cdot \mathbf{n}|_{(\partial\Omega,t)} = 0, \quad \nabla\theta \cdot \mathbf{n}|_{(\partial\Omega,t)} = 0 \tag{17}$$

and the loading conditions for different loading cases are

$$\begin{aligned} \text{Axial : } u_1|_{(\partial\Omega=4,t)} &= d_a, \\ \text{Bending : } u_2|_{(\partial\Omega=4,t)} &= d_b, \\ \text{Multi - axial : } u_1|_{(\partial\Omega=4,t)} &= d_a, \quad u_2|_{(\partial\Omega=4,t)} = d_b, \end{aligned} \tag{18}$$

where d_a and d_b are the ramp displacement based loading and unloading with axial χ_a and bending χ_b displacements, respectively, as shown in Fig. 2b. The expressions for ramp displacement based loading and unloading are

$$\begin{aligned} d_a &= \chi_a [t_{la} - |(t - t_{sa}) - t_{la}|] \left(\frac{t_{la}}{t_{la} - t_{sa}} \right), \\ d_b &= \chi_b [t_{lb} - |(t - t_{sb}) - t_{lb}|] \left(\frac{t_{lb}}{t_{lb} - t_{sb}} \right), \end{aligned} \tag{19}$$

where t_{sa} and t_{sb} are the start of loading times, t_{la} and t_{lb} are the loading times to reach χ_a and χ_b

displacements for axial and bending loadings respectively. Next, we conducted the numerical experiments on the evolved nanowire in twinned martensite and austenite from the previous section.

3.2.1 Nanowire with twinned microstructure as an initial condition

Here, we first present the results of first three experiments in Table 1 reported in [56] for the sake of completeness and then discuss the complex multi-axial loading experiments carried out additionally to understand the dynamic thermo-mechanical properties of SMA nanowires.

The nanowire with evolved twinned microstructure, as shown in Fig. 3a, is used as an initial condition for the multi-axial loading experiments. The nanowire is loaded in the axial (experiment 1), bending (experiment 2), and multi-axial (experiment 3) directions as mentioned in Table 1. The simulations are performed for each loading case individually. We presented the results of the above three experiments in Dhote et al. [56]. In axial loading, the twinned microstructure is converted to a favorable martensitic phase (M+) to the axial loading via a process of detwinning, as also reported experimentally [78]. The elastic loading and phase transformations occur simultaneously. In the case of bending load, the phase transformations occur in a localized area and the redistribution of martensitic domains has been observed. The redistribution of martensitic domains is governed by the local axial stress sign. The phenomenon of redistribution of martensite has also been experimentally reported by Rejzner et al. [79] in Cu- based SMAs subjected to pure bending. In the multi-axial case (experiment 3), the mixed behavior of elastic loading, detwinning, and redistribution of martensitic domains is observed. The simultaneous occurrence of these phenomena affects the mechanical properties of SMA nanowires.

The microstructures evolution has been quantitatively studied by comparing the normalized area of

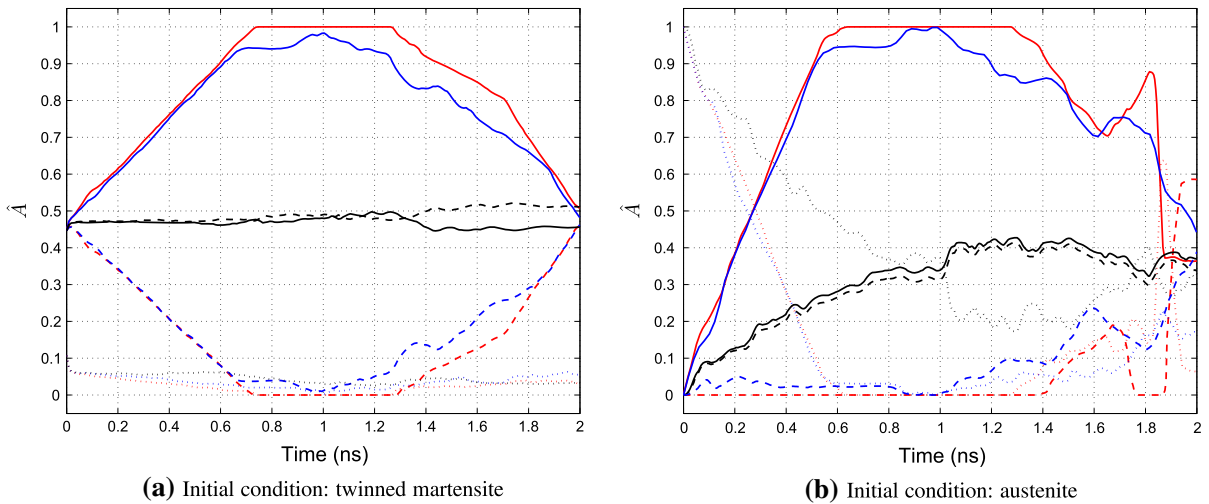


Fig. 4 (Color online) Evolution of \hat{A}_\square with time starting from initial **a** twinned martensite and **b** austenite conditions for different loading cases: axial (red), bending (black), and multi-

axial (blue) (solid lines represent \hat{A}_{M+} , dash lines represent \hat{A}_{M-} , and dotted line represent \hat{A}_A).

different phases in the domain by defining the parameter \hat{A}_\square as

$$\hat{A}_\square = \frac{\text{Area of martensite or austenite phase}}{\text{Area of the nanowire}}, \quad (20)$$

where \square refer to $M+$ and $M-$ variants and A phase.

Figure 4a shows the evolution of \hat{A}_\square for the three loading cases mentioned above. The observations of elastic loadings, phase transformations, and redistribution of martensites under different loading conditions has also been predicted from the Fig. 4a.

The axial stress–strain behavior of nanowires for the axial (experiment 1) and multi-axial (experiment 3) case (refer to solid and dotted lines) is shown in Fig. 5a. In the multi-axial loading case, the shear strains are non-zero and are coupled with the axial components of deformation. The stress–strain characteristics of nanowire under multi-axial loadings are quite distinct as compared to the uniaxial loading and the particular stress level is reached at a lower strain. The existing variants lead to higher stresses due to a higher energy state of multi-axial loading. The temperature evolution for different loading cases (refer to the solid lines) is shown in Fig. 5b. The increase and decrease of temperature upon loading and unloading has been verified experimentally by the works of Gadaj et al. [68] and Pieczyska et al. [69, 70]. The temperature

increase in the bending case is not steep as compared to the axial case because the variants are redistributed in a domain.

The above experiments provide insight into the response of nanowire subjected to dynamic axial, bending, and multi-axial loadings. Further new sets of simulations have been carried out with complex multi-axial loading patterns to study nanowire response. The nanowires have been subjected to different complex multi-axial loading cases—experiments 4, 5, and 6 (refer to Table 1). These experiments refer to the application of bending loads with different χ_b, t_{sb}, t_{lb} . The time-snapshots of microstructure evolution for three multi-axial experiments are shown in Fig. 6a–c. It is observed that the dynamics of loading causes the evolution of microstructures in different patterns. The axial stress–strain curves for three experiments are shown in Fig. 7a. A significant difference in response of nanowires to dynamic loadings is evident from the variation in stress–strain curves for complex loading cases. The sudden application of bending load causes increased (sudden jump in) axial stiffness of the nanowire, which reduce subsequently as the deformation wave travels and the load is distributed in the whole domain. The combination of magnitude of χ_b and its loading–unloading duration t_{sb}, t_{lb} would dictate the dynamics of elastic

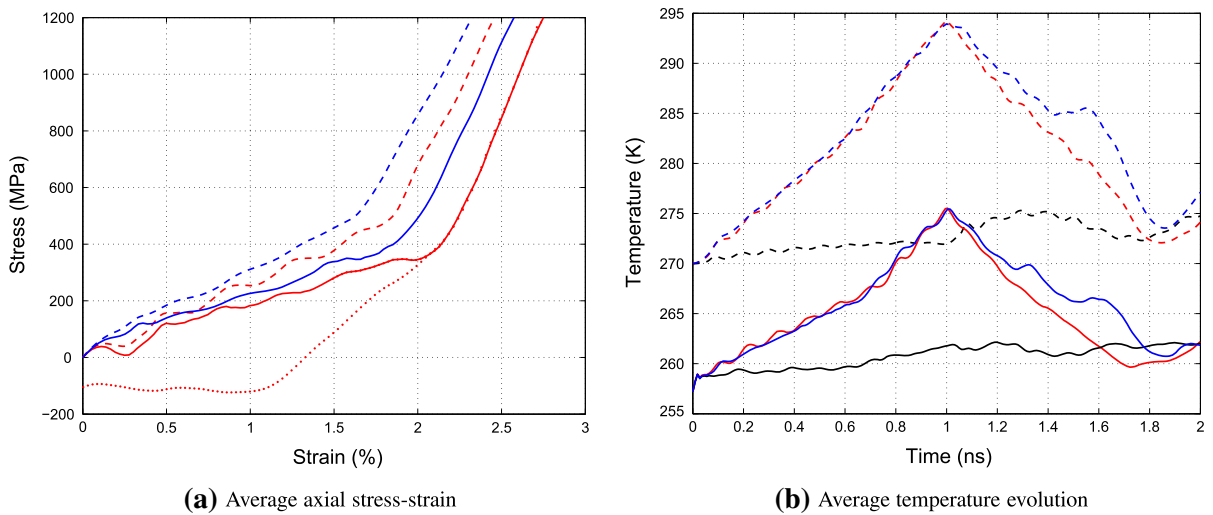


Fig. 5 (Color online) Average **a** axial stress–strain and **b** temperature evolution for different loading cases: axial (red), bending (black), and multi-axial (blue) for nanowire

initially in **a** twinned phase (solid lines) [56], and **b** austenite phase (dashed line). The dotted line in **a** represents unloading of the twinned phase

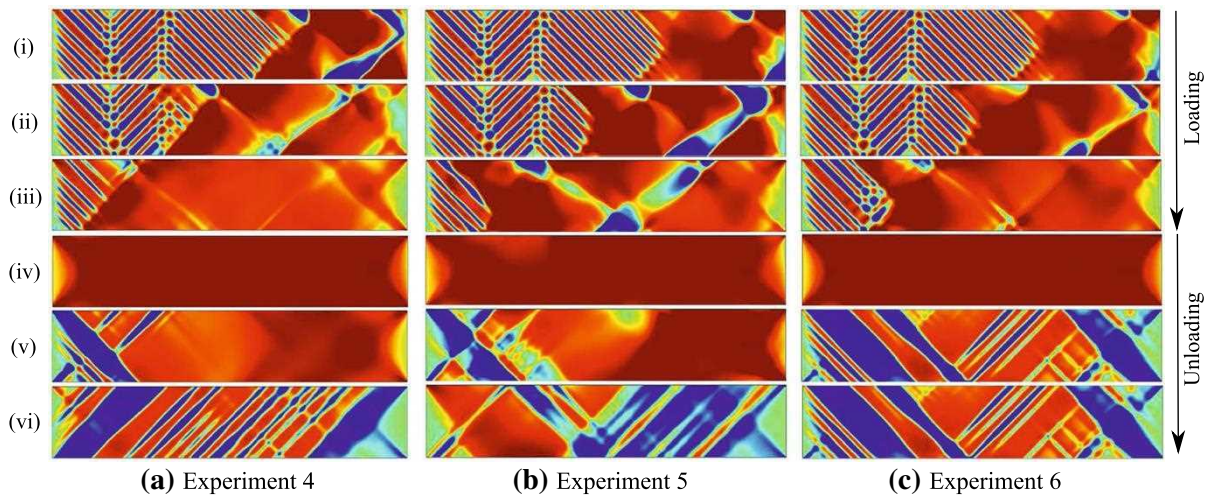


Fig. 6 (Color online) Evolution of microstructure in the (twinned phase) nanowire subjected to multi-axial loading and unloading in **a** experiment 4, **b** experiment 5, and **c** experiment 6

at time (ns) (i) 0.25, (ii) 0.375, (iii) 0.5, (iv) 1.0, (v) 1.5, and (vi) 2.0 (red and blue indicate martensite variants and green indicates austenite)

loading, phase transformation, and redistribution of martensitic domains. The combined effect of these phenomena is evident from the waviness in \hat{A}_{\square} in Fig. 7b as compared to the microstructure evolution in simple multi-axial experiment (experiment 3) in Fig. 4b. The effect of complex loading characteristics on temperature evolution dynamics is apparent from Fig. 7c.

3.2.2 Nanowire with austenite microstructure as an initial condition

We also conducted the numerical simulations with nanowire in the austenite phase. The microstructure evolution during the axial (experiment 1), bending (experiment 2), and multi-axial (experiment 3) loadings are presented in Fig. 8(a–c). It is observed that the

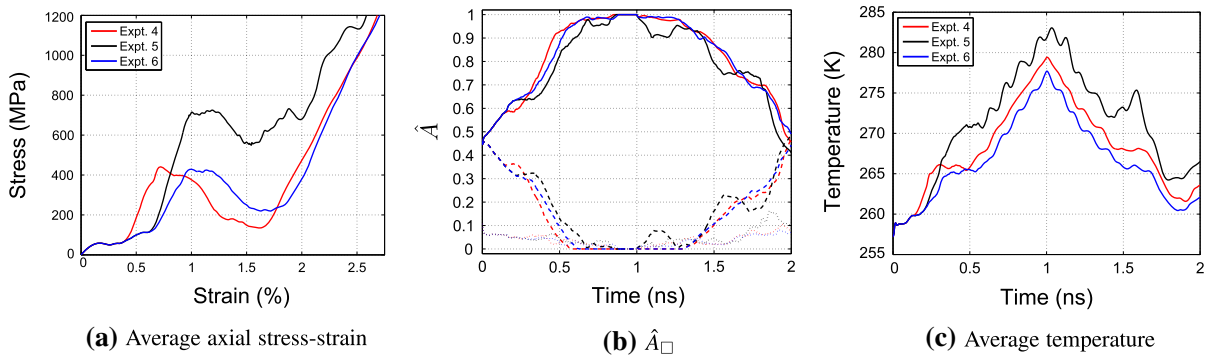


Fig. 7 (Color online) Evolution of **a** average axial stress–strain and **b** \hat{A}_{\square} , and **c** temperature over time for experiment 4 (red), 5 (black), and 6 (blue) for nanowire initially in the twinned phase

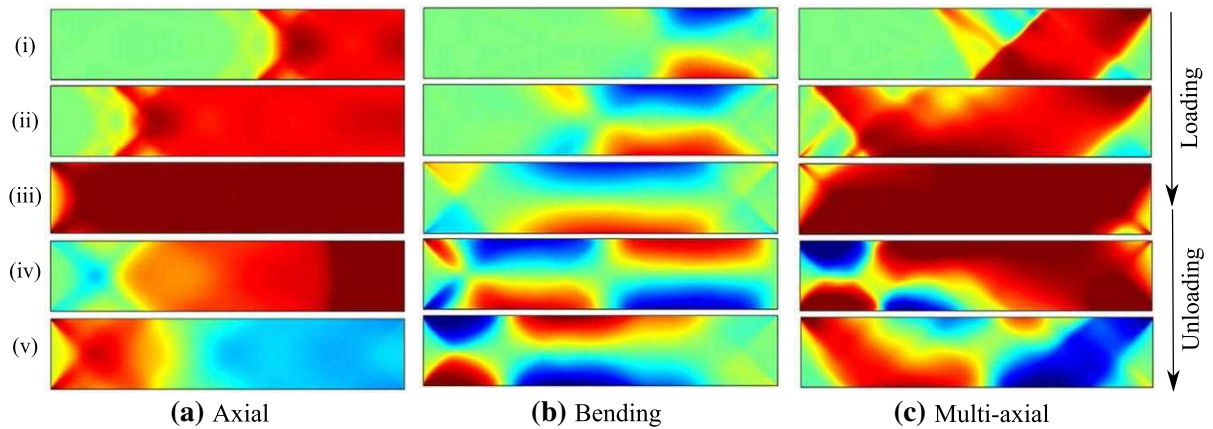


Fig. 8 (Color online) Evolution of microstructure in the (austenite phase) nanowire subjected to **a** axial (experiment 1), **b** bending (experiment 2), and **c** multi-axial (experiment 3)

nanowire in austenite phase is transformed into the favorable martensite upon loadings. This transformation from austenite phase to favorable martensites, via a movement of the habit plane in a nanowire domain, is different from the detwinning transformation described in Sect. 3.2.1. The movement of habit plane is also interpreted from phase change from $\hat{A}_A \rightarrow \hat{A}_{M+}$ with traces of \hat{A}_{M-} during loading as shown in Fig. 4b. An important note to make here is that the \hat{A}_A has significant presence in the domain at the end of unloading. The axial stress–strain behavior of nanowire for axial and multi-axial experiments are shown in the Fig. 5a (refer to the dashed lines). The stiffness of the nanowire in austenite phase is greater than in the twinned martensite phase, which is also experimentally observed in SMAs [10, 12]. The stress–strain

loading and unloading at time (ns) (i) 0.25, (ii) 0.5, (iii) 1.0, (iv) 1.5, and (v) 2.0 (red and blue indicate martensite variants and green indicates austenite)

characteristics of nanowire upon multi-axial loadings are also quite distinct than in the case of the uniaxial loading, and the particular stress level is reached at a lower strain. The evolution of temperature in the nanowire is shown in Fig. 5a (refer to the dashed lines). The microstructure evolution is in qualitative agreement with the axial and bending loading experiments on the NiTi tube [80].

Further, we carried out multi-axial loadings on SMA nanowires with different loading conditions described in experiments 4–6 in Table 1. The time snapshots of microstructure evolution are presented in Fig. 9. The evolution of microstructure distribution \hat{A}_{\square} indicate the dynamics of phase transformations due to complex loadings, as shown in Fig. 10b, and its effect on the evolution of axial stress–strain behavior, and

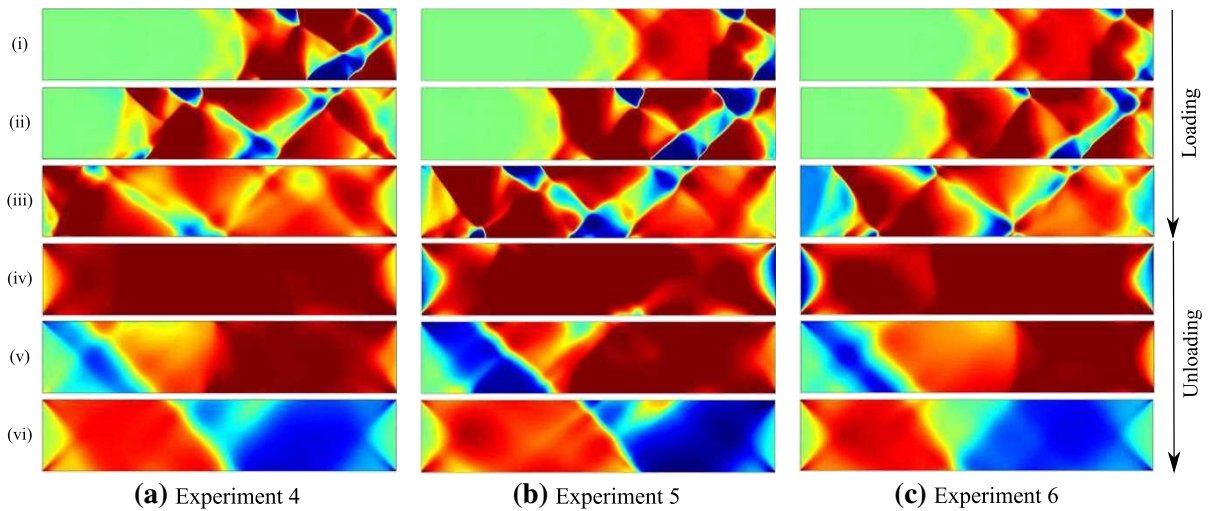


Fig. 9 (Color online) Evolution of microstructure in the (austenite phase) nanowire subjected to multi-axial loading and unloading in **a** experiment 4, **b** experiment 5, and **c** experiment 6 at time (ns) (i) 0.25, (ii) 0.375, (iii) 0.5, (iv) 1.0, (v) 1.5, and (vi) 2.0 (red and blue indicate martensite variants and green indicates austenite)

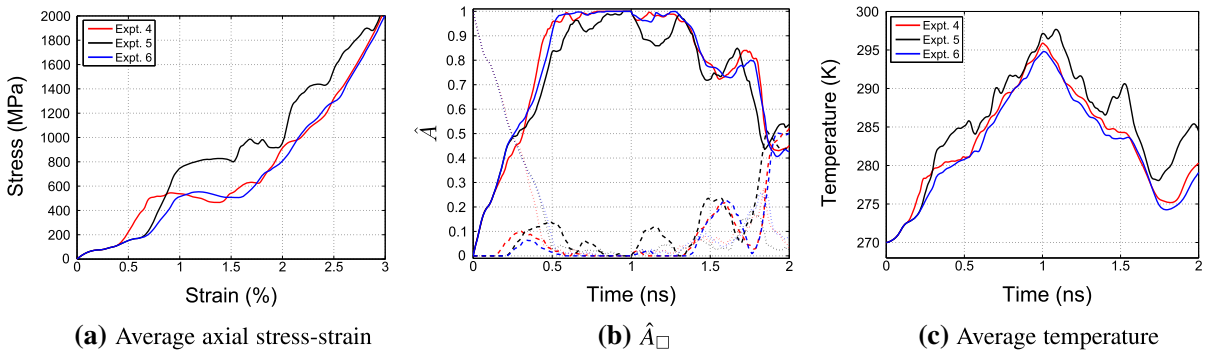


Fig. 10 (Color online) Evolution of **a** average axial stress–strain and **b** \hat{A} , and **c** temperature over time for experiment 4 (red), 5 (black), and experiment 6 (blue) for nanowire initially in the austenite phase

temperature as shown in Fig. 10a, c, respectively. A strong influence of complex multi-axial loading is observed on the dynamics of elastic loading, phase transformation, and redistribution of martensitic domains in SMA nanowire domains. The complex multi-axial loading induces complex thermo-mechanical behaviors in SMA nanowire.

4 Conclusions

We analyzed in detail the thermo-mechanical behavior of FePd nanowires under complex multi-axial loading conditions. The phase-field model with the Ginzburg–Landau free energy was used to model the square-to-

rectangular phase transformations. The simulations were carried out accounting for the coupled thermo-mechanical physics. The numerical results revealed that the axial loading is dominated by the detwinning phase transformation, while the bending case by the redistribution of martensitic variants based on the local axial stress sign. The multi-axial behavior of nanowires is quite distinct as compared to the uniaxial loading due to the combined dynamics of elastic loading, phase transformations, and redistribution of the martensitic variants, with particular stress reaching at a lower strain. The multi-axial loading characteristics causes complex thermo-mechanical behavior of SMA nanostructures. The results of multi-axial behaviors are important in developing better SMA

nanowire based actuators, sensors, as well as in control of MEMS and NEMS devices.

Although the simulations enhanced our understanding of microstructure evolution and its effect on response of the material subjected to dynamic multi-axial loading, there are current limitations in the temporal domain due to model rescaling. Further studies with different boundary conditions and 3D models [81] will provide further insight into the nanowire response to multi-axial loading dynamics.

Acknowledgments RPD, JZ and RNVM were supported by NSERC and CRC program, Canada. RM thanks colleagues at Mevlana University for their hospitality during his visit there and TÜBITAK for its support.

References

- Shu S, Lagoudas D, Hughes D, Wen J (1997) Modeling of a flexible beam actuated by shape memory alloy wires. *Smart Mater Struct* 6:265
- Kahn H, Huff M, Heuer A (1998) The TiNi shape-memory alloy and its applications for MEMS. *J Micromech Microeng* 8:213
- Fu Y, Du H, Huang W, Zhang S, Hu M (2004) TiNi-based thin films in MEMS applications: a review. *Sens Actuators A* 112(2):395–408
- Juan J, No M, Schuh C (2009) Nanoscale shape-memory alloys for ultrahigh mechanical damping. *Nature Nanotechnol* 4(7):415–419
- Barcikowski S, Hahn A, Guggenheim M, Reimers K, Ostendorf A (2010) Biocompatibility of nanoactuators: stem cell growth on laser-generated Nickel–Titanium shape memory alloy nanoparticles. *J Nanopart Res* 12(5):1733–1742
- Bayer BC, Sanjabi S, Baehtz C, Wirth CT, Esconjauregui S, Weatherup RS, Barber ZH, Hofmann S, Robertson J (2011) Carbon nanotube forest growth on NiTi shape memory alloy thin films for thermal actuation. *Thin Solid Films* 519(18):6126–6129
- Bhattacharya K (2003) *Microstructure of martensite: why it forms and how it gives rise to the shape-memory effect*. Oxford University Press, Oxford
- Smith R (2005) *Smart material systems: model development*, vol 32. Society for Industrial Mathematics, Philadelphia
- Lagoudas D, Brinson L, Patoor E (2006) Shape memory alloys, part II: modeling of polycrystals. *Mech Mater* 38(5–6):430–462
- Lagoudas D (2008) *Shape memory alloys: modeling and engineering applications*. Springer, London
- Yoneyama T, Miyazaki S (2008) *Shape memory alloys for biomedical applications*. Woodhead Publishing
- Otsuka K, Wayman C (1998) *Shape memory materials*. Cambridge University Press, New York
- Kohl M (2004) *Shape memory microactuators*. Springer, Berlin
- Miyazaki S, Fu Y, Huang W (2009) *Thin film shape memory alloys: fundamentals and device applications*. Cambridge University Press, Cambridge
- Ozbulut O, Hurlbaeus S, DesRoches R (2011) Seismic response control using shape memory alloys: a review. *J Intell Mater Syst Struct* 22(14):1531–1549
- Elahinia M, Hashemi M, Tabesh M, Bhaduri S (2011) *Manufacturing and processing of NiTi implants: a review*. Prog Mater Sci
- Fang D, Lu W, Hwang K (1998) Pseudoelastic behavior of CuAlNi single crystal under biaxial loading. *Met Mater Int* 4(4):702–706
- Shan Y, Dodson J, Abraham S, Speich JE, Rao R, Leang KK (2007) A biaxial shape memory alloy actuated cell/tissue stretching system. In: ASME 2007 international mechanical engineering congress and exposition, American Society of Mechanical Engineers, pp. 161–169.
- Niendorf T, Lackmann J, Gorny B (2011) H. Maier, *Scr Mater*, In-situ characterization of martensite variant formation in Nickel-Titanium shape memory alloy under biaxial loading. *Scripta Materialia*
- Tokuda M, Petr S, Takakura M, Ye M (1995) Experimental study on performances in Cu-based shape memory alloy under multi-axial loading conditions. *Mater Sci Res Int* 1(4):260–265
- Sittner P, Hara Y, Tokuda M (1995) Experimental study on the thermoelastic martensitic transformation in shape memory alloy polycrystal induced by combined external forces. *Metall Mater Trans A* 26(11):2923–2935
- Lim T, McDowell D (1999) Mechanical behavior of an Ni-Ti shape memory alloy under axial-torsional proportional and nonproportional loading. *J Eng Mater Technol* 121:9
- Bouvet C, Calloch S, Lexcelent C (2002) Mechanical behavior of a Cu–Al–Be shape memory alloy under multi-axial proportional and nonproportional loadings. *J Eng Mater Technol* 124:112
- McNaney J, Imbeni V, Jung Y, Papadopoulos P, Ritchie R (2003) An experimental study of the superelastic effect in a shape-memory Nitinol alloy under biaxial loading. *Mech Mater* 35(10):969–986
- Lavernhe-Taillard K, Calloch S, Arbab-Chirani S, Lexcelent C (2009) Multiaxial shape memory effect and superelasticity. *Strain* 45(1):77–84
- Grabe C, Bruhns O (2009) Path dependence and multi-axial behavior of a polycrystalline NiTi alloy within the pseudoelastic and pseudoplastic temperature regimes. *Int J Plast* 25(3):513–545
- Birman V (1997) Review of mechanics of shape memory alloy structures. *Appl Mech Rev* 50(11):629–645
- Paiva A, Savi M (2006) An overview of constitutive models for shape memory alloys. *Math Probl Eng* 2006:1–30
- Khandelwal A, Buravalla V (2009) Models for shape memory alloy behavior: an overview of modeling approaches. *Int J Struct Changes Solids* 1(1):111–148
- Tokuda M, Ye M, Takakura M, Sittner P (1999) Thermo-mechanical behavior of shape memory alloy under complex loading conditions. *Int J Plast* 15(2):223–239
- Bouvet C, Calloch S, Lexcelent C (2004) A phenomenological model for pseudoelasticity of shape memory alloys under multiaxial proportional and nonproportional loadings. *Eur J Mech-A/Solids* 23(1):37–61
- Thiebaud F, Collet M, Foltete E, Lexcelent C (2007) Implementation of a multi-axial pseudoelastic model to

- predict the dynamic behavior of shape memory alloys. *Smart Mater Struct* 16:935
33. Pan H, Thamburaja P, Chau F (2007) Multi-axial behavior of shape-memory alloys undergoing martensitic reorientation and detwinning. *Int J Plast* 23(4):711–732
 34. Arghavani J, Auricchio F, Naghdabadi R, Reali A, Sohrabpour S (2010) A 3-D phenomenological constitutive model for shape memory alloys under multiaxial loadings. *Int J Plast* 26(7):976–991
 35. Saleeb A, Padula S II, Kumar A (2011) A multi-axial, multimechanism based constitutive model for the comprehensive representation of the evolutionary response of SMAs under general thermomechanical loading conditions. *Int J Plast* 27(5):655–687
 36. Raniecki B, Lexcellent C, Tanaka K (1992) Thermodynamic models of pseudoelastic behaviour of shape memory alloys. *Arch Mech* 44:261–284
 37. Khachaturian A (1983) *Theory of structural transformations in solids*. Wiley, New York
 38. Melnik R, Roberts A, Thomas K (1999) Modelling dynamics of shape-memory-alloys via computer algebra. *Proc SPIE Math Control Smart Struct* 3667:290–301
 39. Melnik R, Roberts A, Thomas KA (2000) Computing dynamics of copper-based SMA via center manifold reduction models. *Comput Mat Sci* 18:255–268
 40. Artemev A, Jin Y, Khachaturyan A (2001) Three-dimensional phase field model of proper martensitic transformation. *Acta Mater* 49(7):1165–1177
 41. Chen L (2002) Phase field models for microstructure evolution. *Annu Rev Mater Res* 32:113–140
 42. Levitas V, Preston D (2002) Three-dimensional Landau theory for multivariant stress-induced martensitic phase transformations. II. Multivariant phase transformations and stress space analysis. *Phys Rev B* 66(134206):1–15
 43. Ahluwalia R, Lookman T, Saxena A (2006) Dynamic strain loading of cubic to tetragonal martensites. *Acta Materialia* 54:2109–2120
 44. Wang L, Melnik R (2007) Finite volume analysis of nonlinear thermo-mechanical dynamics of shape memory alloys. *Heat Mass Transf* 43(6):535–546
 45. Bouville M, Ahluwalia R (2008) Microstructure and mechanical properties of constrained shape memory alloy nanograins and nanowires. *Acta Mater* 56(14):3558–3567
 46. Daghia F, Fabrizio M, Grandi D (2010) A non isothermal Ginzburg–Landau model for phase transitions in shape memory alloys. *Meccanica* 45:797–807
 47. Dhote R, Fabrizio M, Melnik R, Zu J (2013) Hysteresis phenomena in shape memory alloys by non-isothermal Ginzburg–Landau models. *Commun Nonlinear Sci Numer Simul* 18:2549–2561
 48. Idesman A, Cho J, Levitas V (2008) Finite element modeling of dynamics of martensitic phase transitions. *Appl Phys Lett* 93(4):043102
 49. Melnik R, Roberts A, Thomas KA (2002) Phase transitions in shape memory alloys with hyperbolic heat conduction and differential-algebraic models. *Comput Mech* 29(1):16–26
 50. Melnik R, Roberts A (2003) Modelling nonlinear dynamics of shape-memory-alloys with approximate models of coupled thermoelasticity. *Z Angew Math Mech* 83(2):93–104
 51. Mahapatra D, Melnik R (2006) Finite element analysis of phase transformation dynamics in shape memory alloys with a consistent Landau–Ginzburg free energy model. *Mech Adv Mater Struct* 13:443–455
 52. Wang L, Melnik R (2010) Low dimensional approximations to ferroelastic dynamics and hysteretic behavior due to phase transformations. *J Appl Mech* 77:031015
 53. Dhote R, Melnik R, Zu J (2012) Dynamic thermo-mechanical coupling and size effects in finite shape memory alloy nanostructures. *Comput Mat Sci* 63:105–117
 54. Wang L, Melnik R (2007) Thermo-mechanical wave propagation in shape memory alloy rod with phase transformations. *Mech Adv Mater Struct* 14(8):665–676
 55. Melnik R, Wang L (2009) International conference on computational methods for coupled problems in science and engineering coupled problems 2009, CIMNE, Barcelona pp. 1–4.
 56. Dhote RP, Melnik RVN, Zu JW (2011) Dynamic thermo-mechanical properties of shape memory alloy nanowires upon multi-axial loading. *ASME conference on smart materials, adaptive structures and intelligent systems* pp. 411–417
 57. Dhote R, Gomez H, Melnik R, Zu J. 3D coupled thermo-mechanical phase-field modeling of shape memory alloy dynamics via isogeometric analysis (submitted for evaluation, available as arXiv:1403.5612)
 58. Dhote R, Gomez H, Melnik R, Zu J. Shape memory alloy nanostructures with coupled dynamic thermo-mechanical effects, 2014, (available as arXiv:1403.6133)
 59. Falk F (1980) Model free energy, mechanics, and thermodynamics of shape memory alloys. *Acta Metall* 28(12):1773–1780
 60. Carstensen C (1996) On the computational of crystalline microstructure. *Acta Numer* 5:191–256
 61. Rabe K, Ahn C, Triscone J (2007) *Physics of ferroelectrics: a modern perspective*. Springer, Berlin
 62. Clayton JD, Knap J (2011) A phase field model of deformation twinning: nonlinear theory and numerical simulations. *Phys D* 240(9):841–858
 63. Hildebrand F, Miehe C (2012) A phase field model for the formation and evolution of martensitic laminate microstructure at finite strains. *Philos Mag* 92(34):4250–4290
 64. Levin VA, Levitas VI, Zingerman KM, Freiman EI (2013) Phase-field simulation of stress-induced martensitic phase transformations at large strains. *Int J Solids Struct* 50(19):2914–2928
 65. Phillips R (2001) *Crystals, defects and microstructures: modeling across scales*. Cambridge University Press, Cambridge
 66. Clayton JD (2011) *Nonlinear mechanics of crystals*, vol 177. Springer, Dordrecht
 67. Waitz T, Antretter T, Fischer F, Simha N, Karnthaler H (2007) Size effects on the martensitic phase transformation of NiTi nanograins. *Acta Mater* 55(2):419–444
 68. Gadaj S, Nowacki W, Pieczyska E (2002) Temperature evolution in deformed shape memory alloy. *Infrared Phys Technol* 43(3–5):151–155
 69. Pieczyska E, Gadaj S, Nowacki W, Tobushi H (2006) Phase-transformation fronts evolution for stress-and strain-controlled tension tests in TiNi shape memory alloy. *Exp Mech* 46(4):531–542
 70. Pieczyska EA, Tobushi H (2010) Temperature evolution in shape memory alloy during loading in various conditions. 10th international conference on quantitative infrared thermography, pp. 1–6.

71. Ricci A, Ricciardi A (2010) A new finite element approach for studying the effect of surface stress on microstructures. *Sens Actuators A* 159:141–148
72. Comsol Multi-Physics Modeling and Simulation Software (2012). URL <http://www.comsol.com>. Accessed May 2013
73. Park K, Banerjee P (2002) Two- and three-dimensional transient thermoelastic analysis by BEM via particular integrals. *Int J Solids Struct* 39(10):2871–2892
74. Wang L, Melnik R (2006) Differential-algebraic approach to coupled problems of dynamic thermoelasticity. *Appl Math Mech* 27(9):1185–1196
75. Sapriel J (1975) Domain-wall orientations in ferroelastics. *Phys Rev B* 12(11):5128
76. Yasuda H, Komoto N, Ueda M, Umakoshi Y (2002) Microstructure control for developing Fe–Pd ferromagnetic shape memory alloys. *Sci Technol Adv Mater* 3(2):165–169
77. Ma Y, Setzer A, Gerlach JW, Frost F, Esquinazi P, Mayr SG (2012) Freestanding single crystalline Fe–Pd ferromagnetic shape memory membranes—role of mechanical and magnetic constraints across the martensite transition. *Adv Funct Mater* 22(12):2529–2534
78. Liu Y (2001) Detwinning process and its anisotropy in shape memory alloys. *Smart materials and MEMS*, International Society for Optics and Photonics, pp. 82–93.
79. Rejzner J, LExcellent C, Raniecki B (2002) Pseudoelastic behaviour of shape memory alloy beams under pure bending: experiments and modelling. *Int J Mech Sci* 44(4):665–686
80. Reedlunn B, Churchill CB, Nelson EE, Shaw JA, Daly SH (2014) Tension, compression, and bending of superelastic shape memory alloy tubes. *J Mech Phys Solids* 63:506–537
81. Dhote R, Gomez H, Melnik R, Zu J (2013) Isogeometric analysis of coupled thermo-mechanical phase-field models for shape memory alloys using distributed computing. *Proc Comput Sci* 18:1068–1076